

Mixing, Entrainment and Fractal Dimensions of Surfaces in Turbulent Flows

K. R. Sreenivasan, R. Ramshankar and C. Meneveau

Proc. R. Soc. Lond. A 1989 **421**, 79-108

doi: 10.1098/rspa.1989.0004

Email alerting service

Receive free email alerts when new articles cite this article - sign up in the box at the top right-hand corner of the article or click [here](#)

To subscribe to *Proc. R. Soc. Lond. A* go to:

<http://rspa.royalsocietypublishing.org/subscriptions>

Mixing, entrainment and fractal dimensions of surfaces in turbulent flows

BY K. R. SREENIVASAN, R. RAMSHANKAR AND C. MENEVEAU
Mason Laboratory, Yale University, New Haven, Connecticut 06520, U.S.A.

*(Communicated by M. V. Berry, F.R.S. – Received 9 November 1987 –
 Revised 16 June 1988)*

[Plate 1]

Some basic thoughts are set down on the relation between the fractal dimension of various surfaces in turbulent flows, and the practically important processes of mixing between two streams (reacting or otherwise) separated by a convoluted surface, as well as of entrainment of irrotational flow by a turbulent stream. An expression based on heuristic arguments is derived for the flux of transportable properties (such as mass, momentum, and energy) across surfaces, and a prediction made on this basis for the fractal dimension of surfaces in fully turbulent flows is shown to be in essential agreement with measurements. It is further shown that this prediction remains robust when corrected for the non-uniform effects along the surface. A related prediction concerning the dependence of mixing on the Reynolds number and the fractal dimension of the surface is substantiated, in the developing as well as the fully developed states, by independent measurements of both the fractal dimension and the amount of mixing between reactants in a temporally evolving countercurrent shear flow.

1. INTRODUCTION

There are many types of surface in turbulent flows. Some examples are the vorticity/no-vorticity interface, iso-velocity or iso-concentration surfaces, surfaces separating two reacting or non-reacting species, and iso-dissipation surfaces. These surfaces are wrinkled over a wide range of scales in high Reynolds number turbulent flows, and one of the general beliefs in turbulence is that the scales of wrinkling are self-similar. This property, namely the existence of a wide range of self-similar scales, is a hall-mark of fractals (Mandelbrot 1982). The expectation is then natural that the surfaces of the type mentioned above are fractal-like. In a previous paper (Sreenivasan & Meneveau 1986, subsequently referred to as I) we showed by measurement on some of these surfaces that they are indeed fractal-like, and obtained their fractal dimensions. But we did not say much about the implications of this finding. The primary purpose of this paper is to demonstrate beyond what was accomplished in I that the mathematical notion of the fractal dimension (Mandelbrot 1982) is useful also in the context of (practically important) physical processes in turbulent flows.

Table 1 summarizes our previous results on the fractal dimension of scalar and

[79]

TABLE 1. SUMMARY OF THE FRACTAL DIMENSIONS OF SCALAR AND VORTICITY INTERFACES IN SEVERAL CLASSICAL TURBULENT FLOWS (FROM I)

flow	fractal dimension of interfaces (surface) by	
	two-dimensional slicing	one-dimensional slicing
boundary layer	2.38 ^a	2.40 ^d
axisymmetric jet	2.35 ^b	2.35 ^d
plane wake	—	2.40 ^d
mixing layer	2.33 ^c	2.40 ^d

^a Single value at some typical location in the outer region.

^b Average over a number of realizations (of the order 10) covering a streamwise extent of 5–30 diameters from the nozzle.

^c Average over a number of realizations (of the order 10) covering approximately a streamwise extent of two large structures.

^d Many realizations, with and without the use of Taylor's frozen flow hypothesis.

vorticity interfaces. Because the accuracy of these measurements is not refined enough to attach significance to minor variations between one flow and another, and one method of measurement and another, we conclude that these surfaces in a variety of flows possess a fractal dimension of 2.35 ± 0.05 . The apparent generality of this result, further substantiated in §4, must have a simple and basic explanation, and a search for it and its usefulness in practical contexts is the pervading theme here. We also discuss new results on the variation of the fractal dimension in developing flows.

The paper is organized as follows. First, we provide a heuristic argument relating the fractal dimension of surfaces to processes such as entrainment and mixing in turbulent flows (§2). We then show in the same section that simple considerations can lead to a prediction, consistent with measurements, of the fractal dimension of surfaces in fully turbulent flows. In §3, we show that a correction to this predicted value because of the highly intermittent nature of the turbulent energy dissipation field is quite small. The necessary background for this is provided in detail in Meneveau & Sreenivasan 1987 (subsequently referred to as II) where we showed experimentally that the dissipation field can be represented by a multifractal, but the most important aspects are explained in §3 in a reasonably self-contained way. Also in §3, we make a prediction on the behaviour of the fractal dimension as a function of Reynolds number in developing flows. We substantiate this prediction in §4, where we also present further measurements of the fractal dimension of surfaces in order to illustrate as well as amplify the work of I; the main point of §4, however, is the substantiation of the results of §§2 and 3 by the measurement of mixing between two reactants in a temporally developing shear flow. We conclude the paper with some general remarks on the usefulness of the present approach (§5).

In Appendix A we demonstrate that, for the limited purposes needed here, the dissipation field in the vicinity of the interface is not different in any significant way from that elsewhere in the flow. From a combination of similarity arguments and experimental data, we estimate in Appendix B the constant of proportionality in the expression for mixing derived in §2.

Readers interested in a detailed discussion of how fractal dimensions may be

measured are referred to I, although some relevant information will be provided in §4. On the subject of fractals itself, the original account of Mandelbrot (1982) is the most useful single source.

2. MIXING AND ENTRAINMENT

2.1. *General*

In this paper, we use the term ‘mixing’ to indicate molecular mixing. Similarly, entrainment is identified with the acquisition of vorticity by an initially irrotational fluid element. There is now considerable evidence (see, for example, Roshko 1976) that the processes of entrainment and mixing are initiated by the large structure. This stage essentially commits a fluid element to further processing by the turbulence strain field and, eventually, by the diffusive action at the molecular level. These later stages do not prescribe the amount of entrainment or mixing, but adapt themselves, in a manner to be explained, to the conditions set by the large scale features of the flow.

To understand mixing and entrainment, it is legitimate to begin by examining the large-eddy end of the processes. One can alternatively concentrate on the small-scale end. The former approach, largely driven by flow visualization emphasizing large eddies in the flow, has yielded interesting results (Broadwell & Breidenthal 1982), but it is useful to remark that the large-scale eddies in a flow are, in some sense, the result of the flow instability and hence are highly configuration-dependent. There is thus less probability in this approach of arriving at conclusions that can be valid generally for all flows. On the other hand, the latter approach emphasizing the later stages of the processes has a much better likelihood of such success. The reason is simply that the small scale features of the flow are, to a first approximation, independent of the configurational aspects of the flow.

Motivated by this thinking, we concentrate on the last stages of the entrainment and mixing processes. It is worth emphasizing that this picture neither implies that the role of large eddies is minimal nor that ‘gradient transport’ as understood in turbulence closure is necessary or correct. One might argue (Broadwell & Breidenthal 1982) on the basis of the failure of previous diffusion models that the present approach is doomed to fail also, but we note that the previous attempts failed because they did not take into account the correct surface area across which diffusion occurs. If one looks at the surface area at the resolution of the large scales, such attempts will no doubt fail. The main point to recognize is that a large increase in surface area results because of small-scale convolutions of surfaces. Our contribution is in recognizing *explicitly* that these scales belong to a hierarchy of self-similar structures that can be described by fractals, and in working out the detailed consequences that follow from there. We picture that the complex dynamics of turbulence manifests itself by way of imparting fractal properties (in a manner to be discussed below) to the surfaces of interest, and that the flux across those surfaces occurring by molecular action, follows the well-established Fick’s law of diffusion. We show that the procedure can be formulated successfully over the entire range of Schmidt numbers.

For illustrative purposes, imagine a surface separating two streams marked by

passive scalars A and B. This surface can be defined in some operationally convenient way, for example as an iso-concentration surface where the relative concentration of A is, say, 0.5. This can be called the interface between A and B. We will estimate fluxes across such interfaces. The precise process of setting up the flux across such surfaces depends in detail on the Schmidt number. Where the Schmidt number is of the order unity, straining due to turbulence and the diffusive action occur simultaneously, whereas the two processes are separated when the Schmidt number differs substantially from unity.

The diffusive flux is equal to the product of the surface area, the gradient normal to the surface and the molecular diffusivity. We estimate in §2.2 the surface area given the knowledge of the fractal dimension, and this type of estimate is generalized to cases of non-unity Schmidt numbers in §2.3. In §2.4 some reasonable estimates for the gradients are developed. These are combined in §2.5 to form estimates for fluxes. In §2.6 the equivalent estimates for fluxes due to the convective action of the smallest eddies are presented. Subsequently, we shall use this information to estimate fractal dimension of surfaces.

2.2. *The fractal dimension of surfaces, and their area*

A procedure for measuring the area of surfaces embedded in three-dimensional space is to count the number $N(r)$ of cubic boxes of size r required to cover the surface. The area then is of the order of $N(r)r^2$. If a surface is a classical one, the above quantity quickly asymptotes to a constant independent of r , and this is the true area of the surface. For a true fractal surface that is contorted with squiggles of ever increasing fineness, the measured area estimates will increase indefinitely with increasing resolution according to a power law (Mandelbrot 1982). If D is the fractal dimension of such a surface, the number of boxes required to cover the surface $N(r)$ and the corresponding area $S(r)$ increases with increasing resolution (i.e. decreasing r) according to the relations

$$N \sim r^{-D}, S \sim r^{2-D}. \quad (2.1)$$

The situation is depicted in figure 1*a*. One of the important properties of the fractal dimension is that it exceeds the topological dimension of the fractal object (Mandelbrot 1982). Thus, $D > 2$ for fractal surfaces.

In all practical circumstances, the scale range over which power laws of the type (2.1) hold is bounded by cut-offs on both ends. For surfaces in turbulent flows, the outer cut-off is expected to occur at scales comparable to the integral scale, L , of turbulence, while the inner cut-off occurs at the smallest dynamical scale. For vorticity interfaces, the appropriate inner scale is the Kolmogorov scale $\eta = (\nu^3/\langle \epsilon \rangle)^{1/4}$, where $\langle \epsilon \rangle$ is the average rate of the turbulent energy dissipation. These aspects were demonstrated in I. Of immediate interest is the inner cut-off. The existence of a finite inner cut-off means that, as the surface area gets measured by covering it with increasingly finer elements, a point is reached at which convolutions of even finer scales no longer exist, so that, thereafter, the area does not increase with increasing fineness of resolution; instead, it will saturate (abruptly in an ideal situation) at the maximum value corresponding essentially to the inner cut-off (figure 1*b*). For surfaces considered in this work, the situation

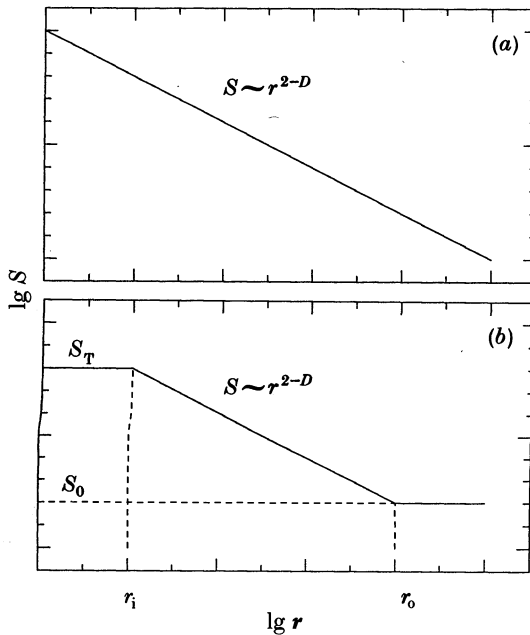


FIGURE 1. (a) The variation of the area S with the resolution r for a fractal surface with no cut-offs. (b) The same variation for a fractal surface with the inner cut-off at r_1 and the outer cut-off at r_0 . The true area S_T of the surface corresponds to the saturation at r_1 .

at the outer cut-off is typically as shown in figure 1*b*, because these surfaces are roughly two-dimensional† when viewed with scales far larger than L . (It is possible to present examples that show other types of behaviour at the outer cut-off, but these counter examples are irrelevant in the present context.) The experimental situation will not be very different, although the transitions are gradual instead of being abrupt as idealized in figure 1*b*. We thus have an interesting situation in which surfaces in turbulent flows look two-dimensional and classical at levels of observation finer than the appropriate inner scale and coarser than the integral scale, but display fractal properties in the intermediate range.

In sum, then, the true area S_T of a fractal surface with finite inner cut-off is given (to within a constant) by the knowledge of the fractal dimension (which gives the slope in the self-similar régime of the line in figure 1*b*), and the inner cut-off r_1 , which theoretically truncates the power-law behaviour. Thus,

$$S_T = S_0(r_1/L)^{2-D}, \quad (2.2)$$

where S_0 is some normalizing area. As mentioned earlier, $r_1 = \eta$ for the vorticity interface. If the area levels off at L and beyond, S_0 becomes the surface area measured with the resolution of L .

† A remark made by Professor Fred Gouldin of Cornell University clarified this situation.

2.3. *The area of surfaces in non-unity Schmidt number flows*

For scalars with Schmidt number ($Sc = \nu/D$, where ν is the kinematic viscosity of the fluid and D is the mass diffusivity of the scalar) far greater than unity, the scales at which diffusivity becomes important are comparable to the Batchelor scale, $\eta_b = \eta Sc^{-\frac{1}{2}}$, which is smaller than the Kolmogorov microscale. There is thus a new scale range ($\eta > r > \eta_b$) in which scale reduction occurs by the action of the strain-rate due to the Kolmogorov-type eddies until scales are reached where the diffusivity effects become directly important. The relevant question now concerns the status of the power law in this range. In analogy with the inertial and viscous-convective ranges in the power-spectral density of passive scalar fluctuations, it is natural to assume that there are two power laws, one governing the range (roughly) $L > r > \eta$, and another in the range $\eta > r > \eta_b$. The two relevant exponents will be called D (in the range $L > r > \eta$) and D' (in the range $\eta > r > \eta_b$). For a fractal surface that exhibits this kind of behaviour, the relation between area and resolution of measurement is shown schematically in figure 2*a*. If S_0 is the area measured with resolution L , S_1 the area measured with resolution η , and S_T is the 'true' area measured with a resolution η_b , we can write

$$S_1 = S_0(\eta/L)^{2-D},$$

and
$$S_T = S_1(\eta_b/\eta)^{2-D'} = S_0(\eta/L)^{2-D}(\eta_b/\eta)^{2-D'}. \quad (2.3)$$

For Schmidt numbers less than unity, the inner cut-off occurs (Corrsin 1964) at $\eta_c = Sc^{-\frac{2}{3}}\eta$, which is larger than η , and the only relevant exponent is D (see figure 2*b*). The true area in this case is given by

$$S_T = S_0(\eta_c/L)^{2-D}. \quad (2.4)$$

2.4. *Estimate for velocity and concentration gradients across surfaces*

Let two streams of the same fluid with velocities U_1 and U_2 (figure 3) be doped by two passive markers A and B. For temporary convenience, let us assume that the species differ in color but possess the same mass diffusivity as the kinematic viscosity of the carrier fluid (that is, $Sc = 1$). Extension to non-unity Schmidt numbers is quite straightforward, and will indeed be done. It is clear that the interface between the two fluid streams is initially of the order of a few mean free paths in thickness, but grows with time like $(\nu t)^{\frac{1}{2}}$, where t is the time since the two streams came in contact with each other. Interfaces of this sort are dynamically unstable (the Kelvin–Helmholtz instability), and roll up into vortex structures as shown schematically in figure 4*a*. These structures bodily move the species A and B from one side to another, but molecular mixing still occurs across the surface area, which now is significantly larger compared to the situation in figure 3. A horizontal line intersection of the type shown in figure 4*a*, taken by a 'point' probe moving sufficiently fast, gives a signal qualitatively similar to that given in figure 4*b*. The interface thickness in figure 4*a* is still given by $(\nu t)^{\frac{1}{2}}$, but the time t is set by the balance between the thickening due to viscous diffusion and the straining imposed by the flow eddies. The characteristic time is the inverse rate of strain equal to $\lambda/\Delta U$, where λ is the scale of eddies deforming the interface. The

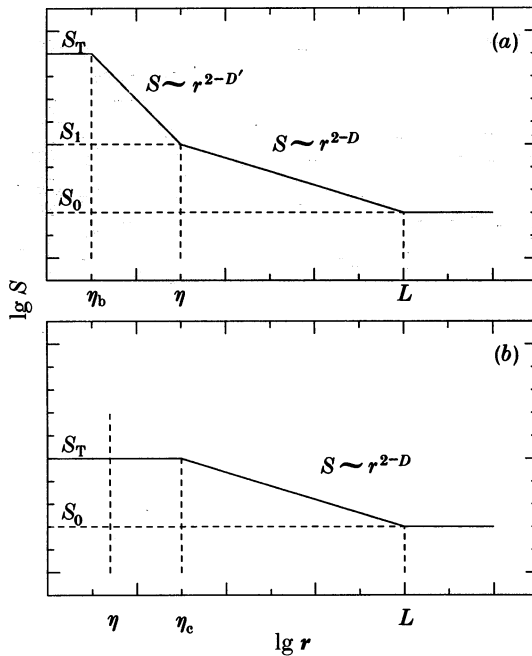


FIGURE 2. (a) The variation of the area S with resolution r for a fractal surface with two different power laws in the two different characteristic scale ranges when $Sc \geq 1$. The true area S_T corresponds to the saturation at η_b . (b) The variation of the area S for $Sc \leq 1$. The true area S_T of the scalar surfaces corresponds to the saturation at η_c .

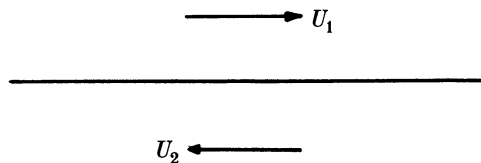


FIGURE 3. The schematic of a countercurrent shear flow before the onset of instability.

characteristic velocity scale ΔU is merely the shear velocity $U_1 - U_2$, and it appears plausible to interpret λ to be of the order of the zero-crossing scale for the signal in figure 4b.

With increasing Reynolds number, small-scale three-dimensional turbulence develops; although the basic two-dimensional structure may still persist (as in this present example), the geometry of surfaces separating the two species (for example the surface on which the mixture fraction is 0.5) is no longer simple. It gets convoluted by a wide range of scales, as shown in figure 5. The inverse rate of strain is now of the order

$$(\nu/\langle \epsilon \rangle)^{\frac{1}{2}} = \lambda/u', \quad (2.5)$$

where $\langle \epsilon \rangle$ is the average rate of dissipation of turbulent energy, λ is the so-called Taylor microscale, and u' is the characteristic fluctuation velocity given by

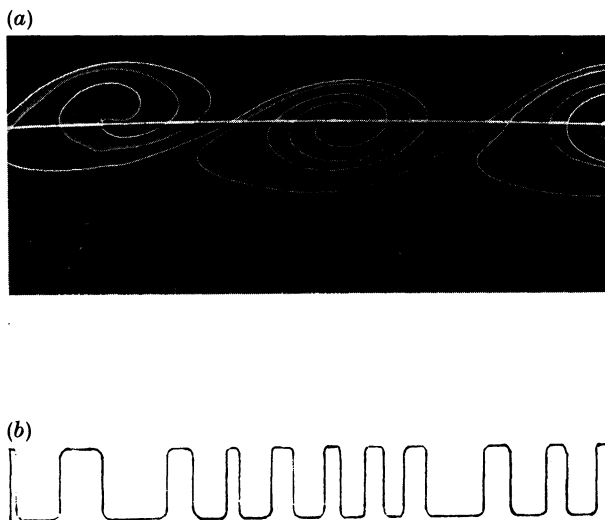


FIGURE 4. (a) Advanced stage of the Kelvin-Helmholtz instability observed in an experiment, and (b) the signal obtained (schematic) by taking the one-dimensional cut through the flow, as shown in (a).



FIGURE 5. Planar intersection of the surface with the mixture fraction 0.5 in a fairly low Reynolds number turbulent mixing layer.

its root-mean-square. Therefore, the thickness[†] of the surface is given by $(\nu\lambda/u')^{\frac{1}{2}} = \lambda(u'\lambda/\nu)^{-\frac{1}{2}} = \eta$. Clearly, these arguments are valid for other flows such as jets, wakes and boundary layers. The characteristic velocity gradient across the interface is of the order U_c/η , where U_c is a characteristic velocity; for example the centreline defect velocity w_0 for the wakes, the centreline excess velocity U_0 for the jets, the velocity difference $U_1 - U_2$ between the two streams for the mixing layer, and the friction velocity U_* (equal in kinematic units to the square root of the wall shear stress) for the boundary layer. It may be of interest to note the

[†] It is possible to justify this estimate by assuming (by analogy with the last statement of the previous paragraph) that the interface is strained by eddies of size comparable to the zero-crossing scale that, according to Sreenivasan, *et al.* (1983), is the Taylor microscale. Although this may make the present estimate more appealing intuitively, a recourse to the existence of an intermediate scale between L and η seems uncalled for and so we prefer the interpretation given in the text. We leave to a later date detailed discussion of the proper place of λ in the hierarchy of scaling.

similarity of the present estimates to those of Tennekes (1968) in a different context of scales of dissipative regions.

Simple extension to high Schmidt number case shows that the characteristic concentration gradient is of the order $\Delta C/\eta_b$, ΔC being a typical concentration difference. For low Schmidt number cases, the appropriate gradient is of the order $\Delta C/\eta_c$.

In the above arguments we have ignored the intermittent nature of the dissipation rate ϵ , whose effects can be seen to appear via (2.5). Furthermore, it is understood that the expressions relating $\langle \epsilon \rangle$, λ , η and u' are also applicable to regions in the neighbourhood of the interface and that these quantities are essentially the same near the interface as everywhere else in the fully turbulent region. In Appendix A we show using experimental data that these assumptions are justified. The correction due to the intermittent nature of ϵ will be discussed in §3.

2.5. Diffusive flux across surfaces

Considering the momentum flux across surfaces, an expression can be written in accordance with the discussion so far as

$$\nu S_T(U_c/\eta). \quad (2.6)$$

Defining the characteristic Reynolds number $Re = u'L/\nu$, we may note that $\eta/L \sim Re^{-\frac{3}{4}}$, and use equation (2.2) for the interface area S_T to write

$$\text{diffusive flux of momentum} \sim S_0 U_c^2 (u'/U_c) Re^{\frac{3}{4}(D-\frac{5}{2})}. \quad (2.7)$$

Note that S_0 , U_c and (u'/U_c) are all independent of Re . For high Schmidt number cases, the corresponding result for the flux of a species with concentration difference ΔC is given by

$$\text{diffusive flux of contaminant} \sim S_0 (U_c \Delta C) (u'/U_c) Re^{\frac{3}{4}(D-\frac{5}{2})} Sc^{0.5(D'-3)}, \quad (2.8)$$

where (2.3) has been used for S_T . For the low Schmidt number cases, using (2.4) for S_T , and noting that the characteristic gradient is $\Delta C/\eta_c$, the corresponding result is:

$$\text{diffusive flux of contaminant} \sim S_0 (U_c \Delta C) (u'/U_c) Re^{\frac{3}{4}(D-\frac{5}{2})} Sc^{\frac{3}{4}(D-\frac{5}{2})}. \quad (2.9)$$

2.6. Convective flux across surfaces

We now estimate the flux across surfaces using an alternative view where the transport can be thought of as occurring because of the convective action of the smallest eddies. The characteristic scales of this 'microscopic' convective motion of the convoluted interface with respect to itself can be estimated on dimensional grounds. For example, Corrsin & Kistler (1955) estimated the propagation velocity to be of the order of the Kolmogorov velocity $v_k = (\nu \langle \epsilon \rangle)^{\frac{1}{4}}$. This estimate is not without its problems, at least partly because (again) one might debate about the precise ϵ to be used, but it should be emphasized that we provide in §3 a different argument and show that the final conclusion does not depend on the details of the Corrsin-Kistler model. The final results are therefore independent of the model.

The flux of momentum given by the product of the surface area and the propagation velocity is the product $U_c v_k S_T$, which, after some rearrangement and the use of (2.2), can be written as

$$\text{convective flux} \approx S_0 U_c^2 (u'/U_c) Re^{\frac{3}{4}(D-\frac{7}{3})}. \quad (2.10)$$

It is interesting and significant that both (2.7) and (2.10) have the same dependence on the Reynolds number and the same prefactor. Therefore, in further discussions we do not explicitly distinguish between the two points of view. We can therefore write, without further qualification, that the

$$\text{momentum flux} = \beta S_0 U_c^2 Re^{\frac{3}{4}(D-\frac{7}{3})}, \quad (2.11)$$

where β is some constant. We shall provide estimates for β in §2.8.

Because of the equivalence between the convective and diffusive effects for the unity Schmidt number, it may be useful to think of the equivalent convective process even for the non-unity Schmidt numbers. If, in this case, we assume that the characteristic propagation velocity of the scalar interface is given by $v_b = \eta_b (v \langle \epsilon \rangle / \nu)^{\frac{1}{2}}$ (which is the ratio between the appropriate length and time scales at the end of the viscous-convective subrange), the corresponding result for the passive contaminant is given by

$$\text{contaminant flux} = \gamma S_0 (U_c \Delta C) Re^{\frac{3}{4}(D-\frac{7}{3})} Sc^{0.5(D'-3)}, \quad (2.12)$$

for $Sc > 1$. Here, γ is another constant. For low Schmidt numbers, simple calculations as before show that the Schmidt number term in (2.12) should be replaced by $Sc^{\frac{3}{4}(D-\frac{7}{3})}$.

2.7. An estimate for the fractal dimension of surfaces

It is well known that all fluxes (mass, momentum, energy) must be independent of Reynolds number in fully turbulent flows: the so-called Reynolds number similarity. (This is merely a statement of the observed fact that the growth rates of turbulent flows of a given configuration are independent of fluid viscosity.) According to (2.11) and (2.12) the Reynolds number similarity requires that

$$D = \frac{7}{3} \quad (2.13)$$

for both the vorticity and scalar interfaces, in rough agreement with experiments (table 1). Note that this result is independent of the Schmidt number.

The result (2.13) is one of the main conclusions of the paper. Because we have not allowed for the possible spatial variations of normal 'concentration' gradients along the interface, this estimate is to be treated as 'typical' at best. One possible correction occurs because the interface thickness and the propagation velocity vary from place to place along the interface. We shall show in the following section that this aspect can be accounted for satisfactorily. Readers interested only in the verification of (2.12) can skip most of §3; for their benefit, we note in advance that the correction to the $\frac{7}{3}$ result is relatively small.

Along the same lines, because the total flux of the contaminant is expected to be independent also of the Schmidt number for high Schmidt numbers, it is seen from (2.12) that $D' = 3$. This is another important conclusion. Figure 6 shows

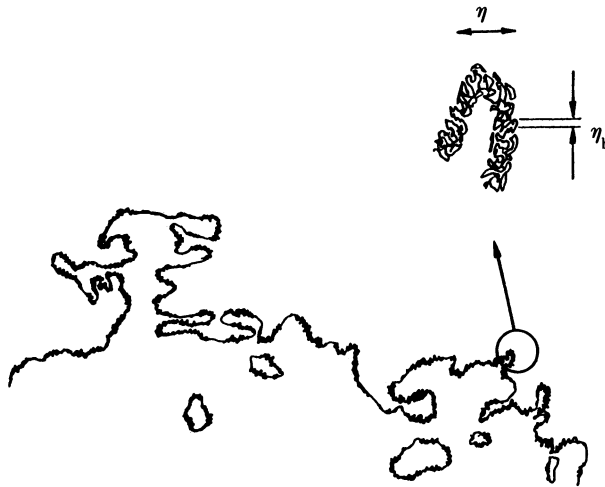


FIGURE 6. Schematic diagram of surface convoluted according to different power-laws in two distinct scale ranges. In the range $L > r > \eta$, the convolutions are self-similar and the surface has a dimension of about $\frac{7}{3}$. The self-similar convolutions of sizes between η and η_b have a dimension 3, practically filling the space.

schematically the convolutions of the interface according to different scales in the large Schmidt number case. The convolutions in the range between L and η are self-similar with a fractal dimension of $\frac{7}{3}$, but those of sizes between η and η_b are much more pronounced; having a fractal dimension of 3, they practically fill the space. Therefore, the effective thickness of the interface appears to be of the order of η even for high Schmidt numbers.

2.8. Entrainment velocity

It is useful to discuss explicitly the entrainment of non-turbulent fluid at the convoluted vorticity interface of a turbulent flow. As a result of the entrainment, the flow grows with downstream distance (or with time, in a temporally growing flow). If the projected area on the x - z plane (in the usual notation; see figure 7) has an area S_p then the so-called entrainment velocity, defined by the identity

$$\text{momentum flux entrained by the turbulent flow} = S_p V_e U_c \quad (2.14)$$

can be estimated by equating this to equation (2.11). Because the ratio of S_p to S_0 can be thought of as a constant for a given flow, a little algebra and some trivial redefinitions lead, for free shear flows, to the expression

$$V_e/U_c = \beta, \quad (2.15a)$$

where the constant β is different for different flows. For the turbulent boundary layer, the corresponding expression can be written as

$$V_e/U_* = \beta(U_*/U_0), \quad (2.15b)$$

where U_0 is the free-stream velocity. The constants β in (2.15a, b) are not known *a priori*, but can be estimated from other considerations. Although they could

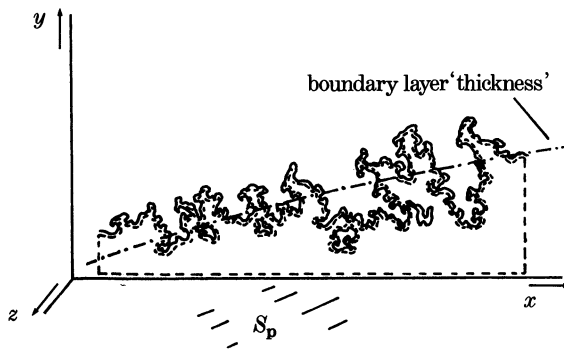


FIGURE 7. Schematic of the vorticity interface in a turbulent boundary layer with x and y axes as defined, the z -axis being the spanwise coordinate. The broken line is a 'control surface' across which momentum balance is made, as described towards the end of §2.8. The projection of the interface on the x - z plane is S_p .

have been estimated in the process of deriving equations (2.11) if we had taken recourse to some level of empiricism, it was felt that, to the extent that some empiricism is unavoidable anyway, the issue should be addressed separately in some unified manner. This is done in Appendix B, but the constants β as well as the characteristic velocities are listed in table 2.

TABLE 2. SUMMARY OF CONSTANTS β IN EQUATION (2.15*a, b*)

flow	U_c	β
plane wake	w_0	0.46
plane jet	U_0	0.10
axisymmetric jet	U_0	0.23
mixing layer	ΔU	0.15
boundary layer	U_*	9

Finally, defining the control volume as shown by the broken line in figure 7 for the turbulent boundary layers, the application of the momentum theorem shows that, to within a constant, the right hand side of (2.11) is also the wall shear force. This, of course, is true as an identity: $\tau_w = U_*^2$ (in kinematic units).

3. FLUCTUATIONS IN THE INTERFACE THICKNESS AND PROPAGATION VELOCITY, AND THE RESULTING CORRECTION TO THE FRACTAL DIMENSION

The correction to be considered here arises from the fact that the energy dissipation fluctuates intermittently in space (Batchelor & Townsend 1949), which in turn induces fluctuations in the rate of strain, as well as both η and v_k . For future reference, we may note that η , v_k , as well as the square root of the rate of strain all depend on quarter powers of the dissipation rate, ϵ . The procedure for correction is simply to replace the average η in (2.6) by the local fluctuating η , and average the gradient estimate U_c/η over the entire domain of the surface; similar

strategy holds also for v_k in §2.6. Alternatively, one can consider fluctuations in the rate of strain in a similar fashion.

Consider briefly the nature of fluctuations of ϵ ; we will use concepts and experimental results described in detail in II. To illustrate the main point of intermittency effects, we have chosen the turbulent wake of a circular cylinder, but the arguments and conclusions hold for the other flows as well. Figure 8 shows a time series of $(\partial u/\partial t)^2$ obtained from a velocity signal $u(t)$ measured in the wake. (The experimental setup is rather standard, and is described in II. As in II, we argue that $(\partial u/\partial t)^2$ can be considered as a reasonable approximation for the rate of dissipation ϵ .) We see from figure 8 that a clustering phenomenon is present, that is, regions where ϵ is almost zero are followed by clusters of high levels of ϵ . These clusters in turn consist of subclusters that are interspersed between regions of low dissipation. The self-similarity of such clusters will induce a series of power laws as will be exemplified below, this being the compelling reason for expecting the fractal behaviour. (That this self-similarity is not global is the reason for expecting the multifractal behaviour described very briefly below; see Mandelbrot 1974, Frisch & Parisi 1985, and II.)

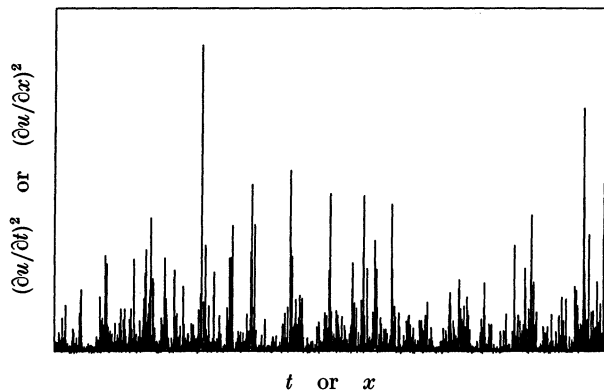


FIGURE 8. A segment of $(\partial u/\partial t)^2$ measured in the turbulent wake of a circular cylinder. This signal can be considered as representative of ϵ , the rate of dissipation of turbulent kinetic energy. Invoking Taylor's frozen-flow hypothesis, this can be viewed as a spatial one-dimensional cut in the coordinate x through the flow-field. The x -axis is divided into equal segments of size r , and ϵ is averaged in each of these boxes, giving ϵ_r . This procedure is repeated for different sizes r to obtain the generalized dimensions D_q (see text and equation (3.1)).

Let us now divide the abscissa in figure 8 into contiguous boxes of size r and focus on ϵ_r , which is the rate of dissipation ϵ averaged over boxes of size r . Clearly, ϵ_r varies from one box to the other. If the boxes are very small, say of size η , ϵ_η will approximate very well the actual dissipation rate ϵ , and so ϵ_η fluctuates greatly from one box to another. On the other hand, if we average ϵ over boxes that are as large as (say) the integral length scale L , we get $\epsilon_L \sim \langle \epsilon \rangle$. Interesting phenomena appear if we consider boxes of sizes lying between η and L . It is clear that as r gets smaller, the variance of ϵ_r gets larger.

We next consider the question of how the moments of ϵ_r depend on r . In general,

the experiments (discussed in greater detail in II) are consistent with power laws that can be written as

$$\langle \epsilon_r^q \rangle = \epsilon_L^q (\mathbf{r}/L)^{(q-1)(D_q-1)}, \quad (3.1)$$

where we have made use of the so-called ‘generalized dimension’ D_q of linear intersections of the dissipation field. These dimensions are in general a function of q (q can be any real number) and play an important and general role in characterizing the multifractal measures (see Mandelbrot 1974, Hentschel & Procaccia 1983, and II). This method of writing the moments of ϵ_r can be thought of as a generalization of the familiar special case for the second moment of ϵ_r (Kolmogorov 1962)

$$\langle \epsilon_r^2 \rangle = \epsilon_L^2 (\mathbf{r}/L)^{-\mu}, \quad (3.2)$$

where μ is the well-known intermittency exponent. We immediately recognise that $\mu = 1 - D_2$. It also follows from the above discussion that the dimension D_0 (for $q = 0$) represents the fractal dimension of the set of points where dissipation occurs in the linear section. The fact that a power law holds means that there is no preferred length scale within the scale-similar range, and thus the variance increases continuously and monotonically as the scale \mathbf{r} becomes smaller.

One can use equation (3.1) or its variants to measure this set of exponents D_q from a time series of ϵ like figure 8 by averaging powers of ϵ_r using boxes of different sizes \mathbf{r} and by identifying the slopes of linear regions in plots of $\lg \langle \epsilon_r^q \rangle$ against $\lg \mathbf{r}$. This was done in II, and the behaviour of the function D_q with q was shown to be a universal property of dissipation in fully turbulent flows, independent of the type of flow as well as the Reynolds number (as long as it is sufficiently high). Figure 9 shows the resulting mean D_q curve obtained in II.

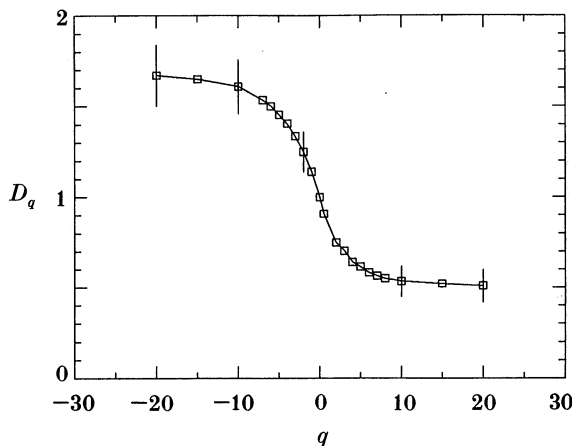


FIGURE 9. The generalized dimensions for one-dimensional sections through the dissipation field in several fully developed turbulent flows (grid turbulence, wake of a circular cylinder, boundary layer, atmospheric turbulence). The experimental details are standard, and can be found in II. The symbols and the continuous curve correspond to the experimental mean, (which is independent of the type of flow within experimental accuracy), and the error bars (also independent of the type of flow) correspond to the variability of the D_q observed at different regions of the time series (these regions being several tens of the integral length scale L) and/or in different realizations of the experiments.

As already mentioned, our interest is in estimating the fluxes allowing for the variability in the Kolmogorov thickness and velocity. That is, instead of using the average η in equation (2.6), and the average v_k in the convection flux estimates, we take the spatial average of the flux after inserting the local unaveraged value of η and v_k . (Because both η and v_k depend on the same quarter power of the dissipation rate, the correction for both quantities is the same.) This operation reduces to replacing $\langle \epsilon \rangle^{\frac{1}{4}}$ by $\langle \epsilon^{\frac{1}{4}} \rangle$. Noting from (3.2) that, for $q = \frac{1}{4}$,

$$\langle \epsilon^{\frac{1}{4}} \rangle \sim \langle \epsilon^{\frac{1}{4}} \rangle = \epsilon_L^{\frac{1}{4}} (\eta/L)^{\frac{3}{4}(1-D_1)}, \quad (3.3)$$

it is straightforward to write, instead of (2.11), that the

$$\text{momentum flux} = \beta S_0 (\Delta U)^2 Re^{\frac{3}{4}[D - \frac{7}{3} - \frac{3}{4}(1-D_1)]}. \quad (3.4)$$

If we use the Reynolds number similarity as before, we get

$$D = \frac{7}{3} + \frac{3}{4}(1 - D_1). \quad (3.5)$$

From our measurements in II (see figure 9) we know that $D_1 \approx 0.97$, and therefore $D = 2.356$, which does not change much the uncorrected value of $\frac{7}{3}$. It is worth emphasizing that the reason for the relatively small correction is that the interface thickness and the propagation velocity depend on the quarter power of the dissipation, and so the strong variabilities in ϵ do not result in comparable variations in η and v_k .

In a similar vein, one can also produce a simple alternative scheme for estimating flux across fractal interfaces in a way that does not depend on the details of the Corrsin–Kistler model. From dimensional considerations, one can write the flux of a contaminant (for simplicity the case of unity Schmidt number) to be

$$\text{flux} = S_T \langle \Delta u_r \rangle \Delta C, \quad (3.6)$$

where Δu_r is a characteristic velocity difference between two points at a distance r across the interface and $\epsilon = O((\Delta u_r)^3/r)$, where (roughly) $\eta < r < L$. Because the interface thickness is of the order η (see §2.4),

$$\langle \Delta u_r \rangle = \langle \Delta u_r \rangle \approx \langle (\epsilon \eta)^{\frac{1}{3}} \rangle. \quad (3.7)$$

But, from (3.1), we have

$$\langle (\epsilon \eta)^{\frac{1}{3}} \rangle \sim (\eta/L)^{\frac{1}{3} + \frac{3}{4}(1-D_1)} \quad (3.8)$$

which allows us to rewrite (3.6), after some algebra, as

$$\text{flux} = S_0 U_c \Delta C (u'/U) Re^{\frac{3}{4}[D - \frac{7}{3} - \frac{3}{4}(1-D_1)]}. \quad (3.9)$$

Again invoking Reynolds number similarity in (3.9), we have

$$D = \frac{7}{3} + \frac{3}{4}(1 - D_1). \quad (3.10)$$

From measurement, $D_1 \approx 0.96$, so that $D \approx 2.36$, not very different from the previous estimate.†

† Although the estimates (3.5) and (3.10) are practically the same numerically, the two are self-consistent only in the space-filling case, that is $D_q = 1$ for all values of q . If, in (3.8), we take into account the fluctuations in η , we get the same result as equation (3.5).

The corrected fractal dimension for the scalar interface is very close to the value measured in I, the results from which are summarized in table 1. This is also close to some new measurements to be presented (in the next section) for mixing layers in the developing as well as fully developed states.

A primary reason for deriving (3.10) in that particular form is to correlate it in §4 with measurements on the Reynolds number variation of the fractal dimension. This comparison is most conveniently made by noting that the inertial-type arguments in turbulence imply that the structure function $\langle |\Delta u_r| \rangle$ varies like r^ξ . It is shown in II that ξ is given by the equation

$$\xi = 1 - \frac{2}{3}D_{\frac{1}{3}}, \quad (3.11)$$

which, with (3.10), can be written as

$$D = 2 + \xi. \quad (3.12)$$

The fractal dimension is thus intimately related to the scaling exponent of the structure function. We shall verify this result by comparing our measurements of D with those of Tong & Goldburg (1988) on the variation of ξ with Reynolds number for developing flows. Their measurements of ξ with photon-correlation spectroscopy showed that it is zero for low Reynolds numbers before the onset of transition to turbulence, and that it asymptotes to a value near $\frac{1}{3}$ at high Reynolds number. This implies, from (3.12), that $D = 2$ for low Reynolds numbers (smooth surfaces before transition), and that it should asymptote to a value near $\frac{7}{3}$ at high Re . We have already deduced and substantiated this last result, and present the remaining results in the following section.

4. EXPERIMENTS IN MIXING LAYERS

4.1. *General remarks*

We showed above that the principle of Reynolds number similarity implies, in agreement with direct measurements, that the fractal dimension of surfaces in fully turbulent flows is about 2.36. Here, we describe some additional results on the measurement of fractal dimensions (§4.2). We also test in a greater detail (§4.3) the validity of equation (2.12) and (3.12) even as transition to turbulence unfolds, and the characteristic flow Reynolds number increases in a developing flow. To do this, we have chosen a temporally developing, countercurrent mixing layer, created as described below. The advantage in the present context of a temporally developing flow over a spatially developing one is that there is in the former an average spatial homogeneity that renders the scale similarity concept more genuine. This can be understood easily. In a spatially developing flow, the scales grow with downstream distance, and so, if one considers a sizeable streamwise cut of an interface, the similarity scale range as well as average inner and outer cutoffs vary from upstream end of the interface section to its downstream end. Even a cursory look at figure 7 will make this obvious. The problem is non-existent in the case of temporally developing flows, thus making it reasonable to expect fractal behaviour to hold there quite strictly.

The countercurrent shear flow was created in a tilting tube apparatus described

by Ramshankar (1988), earlier used in some pioneering experiments by Thorpe (1968); it works on the presence of slight stratification between two layers of fluid in the tube. Briefly, the apparatus is a rectangular plexiglas tube of cross section $5\text{ cm} \times 15\text{ cm}$, and 2.4 m long. The ends of the tube are closed and provided with valves for filling and draining the fluid. During filling the tube from the bottom, the tube is tilted about 60° from the horizontal about its pivot, the light fluid (in this case fresh water) is first introduced at a slow rate, and then the heavy fluid, in this case brine of density 1.02 kg m^{-3} ; care is taken to avoid turbulence and mixing during filling and subsequently tilting the tube back to horizontal. When the small disturbances, unintentionally created during these operations, are brought to rest, the apparatus is ready for the experiment. The density interface formed during this entire procedure is typically 1 mm thick. The countercurrent shear flow is now achieved by tilting the tube by a small angle, thus setting up downward flow of the heavier fluid and upward flow of the lighter fluid (see figure 10); the running time of the experiment is determined by the length of the apparatus, and is typically about 10 s for the present experimental conditions. Even though the flow is slightly stratified, the Richardson number at the onset of instability is low enough (Ramshankar 1988) for it to be considered homogeneous according to a criterion suggested by Koop & Browand (1979). If the tube is maintained in its slightly inclined position, the flow speed (and thus the Reynolds number) increases linearly with time, but the flow can be treated as quasi-steady (Thorpe 1971). The increasing flow speed turns out to be an advantage in the sense that we can have, in the same experimental run, developed mixing layers at increasing Reynolds numbers.

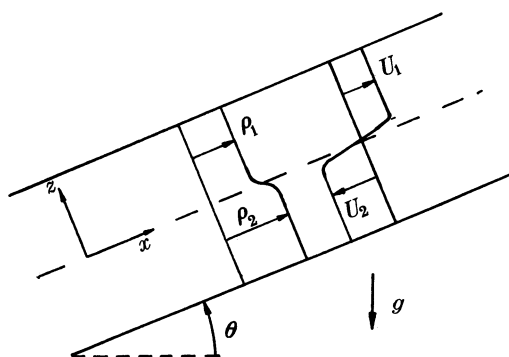


FIGURE 10. Schematic diagram of the flow after it is set up in the tilting tube apparatus. The flow speeds and the total experimental time (for a finite length apparatus) are determined by the tilting angle, which is small (less than 5°) in the present experiments. For the present experiments, the duration of the experiment was about 10 s .

4.2. Measurement of fractal dimension

As mentioned in §4.1, the concepts of fractals are more easily identifiable with flows that have no spatial asymmetry, such as in the countercurrent flow. Figure 11 shows at moderate Reynolds numbers a section of the flow obtained by using laser-induced fluorescence. Here one of the streams is mixed with a

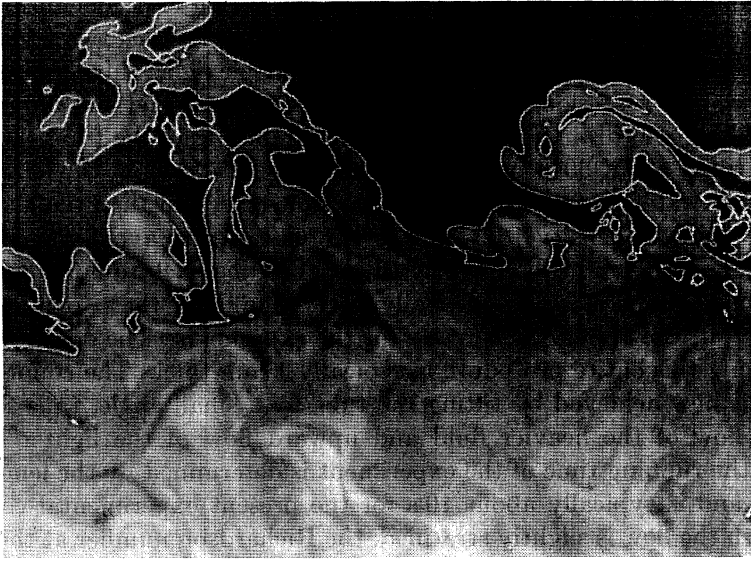


FIGURE 11. Section of a countercurrent flow at a moderate Reynolds number, obtained by using laser-induced fluorescence. Also shown as the white line is the interface drawn by setting a suitable threshold to demarcate the bright regions from the dark.

fluorescing dye and fluorescence is excited by a thin sheet of laser light passing through the mid span of the test section. The thickness of the sheet of laser light is approximately equal to the Kolmogorov microscale η . (This means that we cannot say anything about scales smaller than η .) The image is recorded on a CCD (charge-coupled device) array camera consisting of 1300×1100 pixels and is digitized with a 12 bit digitizer.

Figure 11 also shows the boundary between the bright and dark regions obtained by setting a suitable threshold on the intensity of the image. As can be seen, the method of determining the boundary by setting the threshold is more or less satisfactory; a more thorough investigation by Prasad & Sreenivasan (1988) confirms this conclusion. To the boundary so determined, one can now apply a box-counting algorithm to obtain its fractal dimension. The algorithm consists in covering the whole plane with square boxes of size r and counting the number of boxes $N(r)$ in which the boundary is contained. Because for a fractal object one expects $N(r)$ and r to be related by a power law of the type $N(r) \sim r^{-D}$, a plot of $\lg N(r)$ against $\lg r$ (figure 12) gives us a linear region whose negative slope is the fractal dimension of the boundary shown in figure 11. The result from this realization is approximately 1.35. The number 1.35, however, is the dimension of planar sections of the surface, and not of the surface itself. If we use the additive properties of dimensions governing the intersection of fractals (Mandelbrot 1982, p. 366, and references cited there), the fractal dimension of the surface will be given by $1 + 1.35 = 2.35$. The inset shows that this result is sensibly independent of the threshold over a large fraction of the dynamic range of the signal. This additive procedure, obvious for euclidean objects, is justified also for fractals when the fractal dimension is independent of the orientation of the intersecting plane.

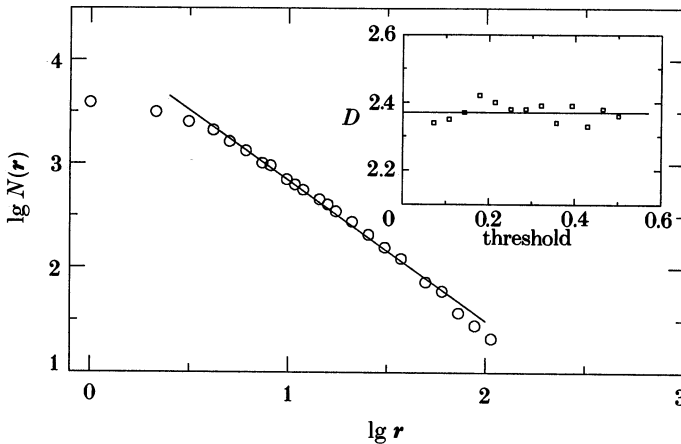


FIGURE 12. Logarithmic plot of $N(r)$, the number of square elements of size r needed to cover the interface shown in figure 11, as a function of r . The slope is -1.35 . Orthogonal sections of the flow yield the same result, and one may therefore conclude that the fractal dimension of the surface is 2.35 (see text). The scaling range is slightly higher than a decade. It is worth pointing out that the scaling range at higher Reynolds numbers is higher. The inset shows the measured dimension as a function of the threshold set on the brightness of the digital image. Here, 0 and 1 correspond to the darkest and brightest pixel intensity in the image. An average value of $D = 2.37$ seems robust. For higher thresholds, the dimension drops off rapidly.

We have made fractal dimension measurements for two orthogonal sections of the flow and confirmed that the result was the same for both.

We now turn to the Reynolds number variation of the fractal dimension of the surface as it evolves from smooth to the fully turbulent state. The sequence of the temporal development of the flow is shown in figure 13, plate 1. Similar procedure as outlined in the previous paragraph was followed, and figure 14 shows the variation of the fractal dimension of the surface with Reynolds number. Following (3.12), we have also compared here the results of Tong & Goldburg (1988) discussed in §3. Their mean curve has been translated to match the critical Reynolds number in our flow; no other adjustable parameters exist in this comparison. The agreement is reasonably good.

4.3. Measurements on mixing

The amount of molecular mixing that occurs between the two streams can be measured at least by two ways. One is the passive scalar technique where an inert scalar such as a dye, premixed with one of the streams, subsequently gets diluted by mixing with the other stream; the dye acts as a conserved scalar. Measuring the local instantaneous concentration of the dye gives a measure of mixing. This scheme, however, has the difficulty that the sampling volume is generally much larger than the smallest scale of turbulence, which for passive mixing is the Batchelor scale. Within the sampling volume it is not possible to determine whether the two streams are mixed or not, and thus the lack of resolution results in the overestimation of the amount of mixing.

Breidenthal (1978) suggested the use of a chemical reaction as an alternative method; Konrad (1976) had earlier advocated the same idea, and used it in gaseous phase. If we have a fast and irreversible reaction of the type $A + B \rightarrow C$, the amount of the product C formed is equal to the amount of molecular mixing between the dilute reactants A and B (at the reaction equivalence ratio) in the two streams. Further, if the product C is visible, a suitable optical method can be used to measure the extent of mixing in a non-intrusive manner. In contrast to the passive scalar method, the finite size of the 'probe' does not cause over-estimation of mixing because the amount of the mixed fluid in an irreversible reaction is exactly equal to the amount of the product that is formed no matter how large the probe volume. For this reason, we present results only for this latter method, although both methods were used (Ramshankar 1988) during the course of this investigation. We shall use as the measure of mixing the so-called 'product thickness' δ_p defined as

$$\delta_p = 1/B_\infty \int_{-\infty}^{+\infty} C(x, y, z, t) dy, \quad (4.1)$$

where B_∞ is the freestream concentration of the species B . The product thickness represents the total amount of product formed when normalized by the freestream concentration of the species involved, chosen arbitrarily as B in the definition (4.1).

4.4. Chemical reaction experiments

A simple acid-base reaction was used here to mark the mixing during the flow. A common pH indicator known as Cresol red, with the property that it is pale yellow in acidic solution and turns deep red when the pH of the medium is raised above 6, was used to indicate the reaction products. Optical techniques based on the attenuation of light by the red product can be used to estimate the extent of mixing. In practice, the reaction used is reversible, and so the extent of mixing obtained by this method is a lower bound in high Schmidt number situations; but this effect can be minimized by using a very large stoichiometric ratio of the reactants.

As mentioned, experiments were conducted in the tilting tube apparatus. Sulphuric acid (pH level of about 5) and the indicator Cresol red were added to the light fluid, and the base (sodium hydroxide, pH level of about 11) to the brine. The optical arrangement consisted of a beam of a mercury vapour lamp that was collimated and spread into a sheet (thickness about 0.5 mm, width exceeding one primary wavelength of the flow instability) using a cylindrical lens. The sheet of light was passed through the tube normal to the plane of the shear layer in the mid-span of the tube. The light sheet was then focused back to a point using a convex lens and a photomultiplier tube was placed at the focal point of the lens (see figure 15). For a given concentration of the red product, the intensity E of the attenuated beam is given by

$$E = E_0 e^{-b\delta_p}, \quad (4.2)$$

where E_0 is the incident light intensity, b is the absorption coefficient of the red product (at the appropriate concentration) and δ_p is the average thickness of the red product in the path of the light. Thus, by recording the attenuation of the light intensity due to the presence of the red product in the light path, and by

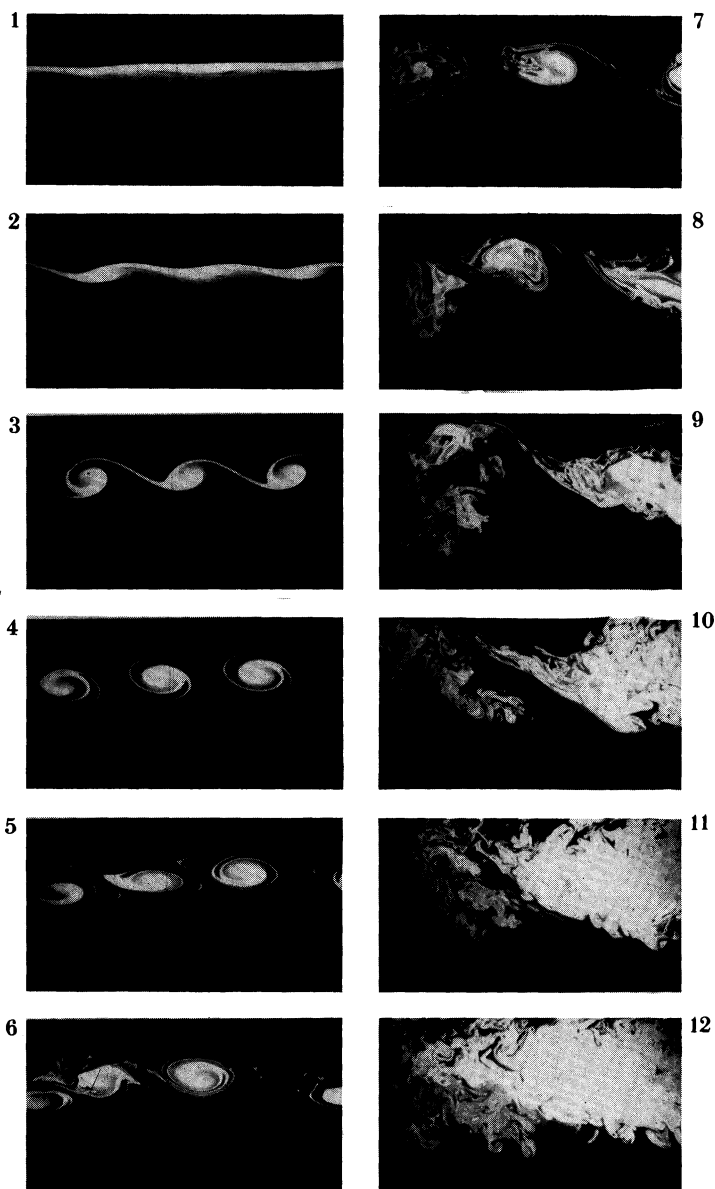


FIGURE 13. Visualization of a thin section of the countercurrent shear flow by laser induced fluorescence at different stages of its evolution. The numbers on these pictures correspond to those on the product thickness curve of figure 17 to follow. Unlike in figure 11, the dye was placed carefully in a thin sheet between the two fluids when filling the tube.

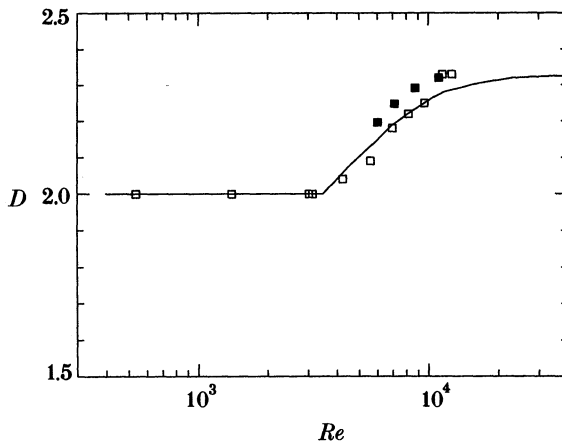


FIGURE 14. The fractal dimension for the dye interface in the countercurrent shear flow. As expected, the fractal dimension increases from 2 in the initial stages (up to somewhere between pictures 3 and 4 in figure 13) to about $\frac{7}{3}$ in the fully developed turbulent region. The onset of three dimensionalities occurs somewhere between the fourth and fifth pictures. The continuous line corresponds to the prediction of D as a function of ξ according to equation (3.12) using experimental data on ξ obtained by Tong & Goldburg (1988). Their mean curve has been translated to match the critical Reynolds number of the present experiment.

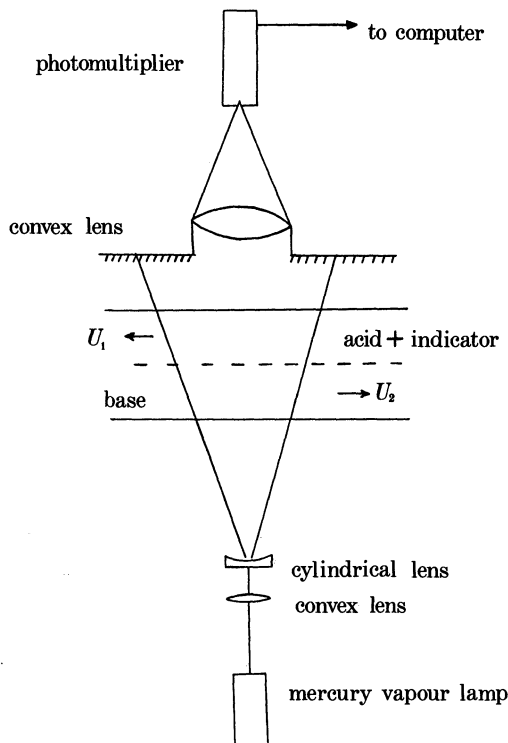


FIGURE 15. Schematic diagram of the apparatus used for measuring product thickness. The scheme is based on Briedenthal's work.

determining via calibration (see below) the attenuation coefficient b , we can obtain the average thickness of the product formed. Because the light sheet passes through the entire cross section of the shear layer, the integration of the local product concentration is already obtained and hence the product thickness defined by equation (4.1) can be obtained. The light intensity at the photomultiplier tube was recorded digitally with and without the red product in the light path; to provide the base level of the product formed, the maximum intensity at the photomultiplier tube was recorded for each run. The data were processed to obtain the product thickness. The low diffusivity of the product ensures that the product thickness measured this way essentially reflects the mixing characteristics corresponding to local conditions alone.

One usual difficulty with the product-thickness measurements in spatially developing mixing layers is the greater tendency of the high-speed fluid to be entrained into the flow. This tendency implies that the amount of product formed depends on whether the acid or base was contained in the high-speed fluid. It must be noted that this difficulty does not exist in the present experiments because the two streams have equal (but opposite) speeds. There is a small amount of asymmetry due to non-unity density ratio (1.03 in most experiments), but this effect was shown to be minimal by Ramshankar (1988) by the so-called 'flip' experiment proposed by Koochesfahani *et al.* (1984).

A few words should be said about the calibration procedure. The attenuation coefficient and the stoichiometric ratio of the reactants were obtained by means of a titration experiment. A known quantity of the acid and the indicator solution is taken in a cuvette cell of known optical path length and the attenuation of the light beam is recorded as the base is added to the cuvette cell. Initially the attenuation is minimal because the red product is not formed but, as more and more acid gets added, there is a sudden enhancement of attenuation, eventually reaching a peak (see figure 16). This peak denotes the reaction stoichiometric ratio. Further addition of the base merely dilutes the product and hence the attenuation is again reduced. The transition of the attenuation as seen can be made very sharp and the stoichiometric ratio can also be altered by simply changing the concentration of the base in the brine solution. The attenuation constant b is then obtained from the equation (4.2) based on the attenuation of the light at the stoichiometric ratio.

4.5. Results

Figure 17 shows the product thickness as a function of flow Reynolds number (which varies with the time measured since setting up the flow). The *approximate* correspondence between the flow structure in figure 13 (from a different run but under nominally the same circumstances) and the mixing data is also shown. It is seen qualitatively that the rapid increase in mixing goes hand in hand with a fairly sudden increase in the complexity of iso-concentration surfaces. Also marked by A is the region of onset of three dimensionalities in the flow, as determined by visual and photographic inspection of the plan view of the flow field. Detailed flow-visualization studies (Ramshankar 1988) support the notion that rapid increase in mixing does not occur until after the onset of three dimensionalities. The product

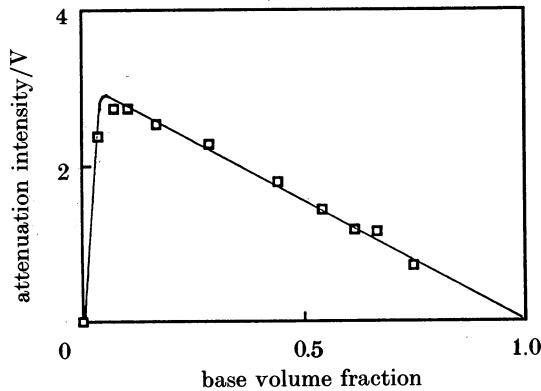


FIGURE 16. Attenuation of light due to the formation of the red product as a function of the base volume fraction. A cuvette cell of known optical path is initially filled with the acid-indicator solution. The attenuation of the light passing through the cuvette cell is recorded in a photomultiplier as the base volume fraction is increased. The attenuation rises sharply to a maximum at the stoichiometric ratio (base volume fraction = $v_b/(v_b + v_a) \approx 0.08$); at this point all of the indicator (Cresol red) is converted to the red product. Further addition of base merely dilutes the red product and hence the attenuation decreases. The attenuation coefficient of the red product at the stoichiometric ratio is then found by using (4.2).

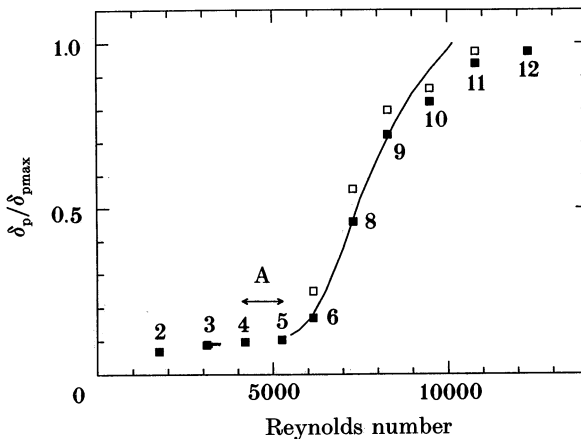


FIGURE 17. The comparison between the measured 'product thickness' (see equation (4.1)) and the prediction (2.12) given by the continuous line, both forced to agree at one point. Open and filled symbols correspond to two different realizations of the flow. The length scale δ_{vis} in the abscissa Reynolds number ($= \Delta U \delta_{vis} / \nu$) is the visual thickness of the countercurrent shear flow. The numbers on the product thickness curve correspond approximately to the sequence of pictures in figure 13.

thickness ratio saturates at about the time when the end-wall effects become important.

Of specific interest here is the comparison between this observed behaviour of mixing and the prediction from equation (2.12). For this purpose, we need to know the dimension of the interface as a function of Reynolds number, and this was

obtained in figure 14. With these data (and $D' = 3$) we may now determine the amount of mixing according to (2.12). In doing so, we replace $u'L/\nu$ in (2.12) by $\Delta U\delta_{\text{vis}}/\nu$, where δ_{vis} is the (measured) visual thickness of the flow. This redefinition of Reynolds number is equivalent to replacing the relation $\eta/L = (u'L/\nu)^{-\frac{2}{3}}$ by $\eta/\delta_{\text{vis}} = (\Delta U\delta_{\text{vis}}/\nu)^{-\frac{2}{3}}$. Measurements in spatially developing mixing layers support the latter relation in the same way that the former is supported by grid turbulence measurements. We determined ΔU from the theoretical analysis of Thorpe (1968, 1971), which gives $\Delta U = 2\zeta g t \sin \theta$, where ζ is the density difference ratio between the two streams, and t is the time since the tank gets tilted to an angle θ to the horizontal.

As emphasized earlier, equation (2.12) is expected to be valid once self-similarity sets in; it is reasonable to think that this occurs, in general, not long after the onset of three dimensionalities. This was definitely the case in our experiments. There is therefore enough justification to use (2.12) in the region to the right of A in figure 17. Because the constant β in (2.12) is unknown (and will remain unknown until the problem is solved in full), we cannot make comparison of absolute values. The comparison with the product thickness, when both quantities are made to agree at $\delta_p/\delta_{p\text{max}}$ of 0.5, appears to be quite reasonable up to the highest Reynolds number for which the flow has not been significantly affected by the end walls of the tilting tube apparatus. At this point, the experiments start to level off but the theoretical estimates do not because the above estimate of ΔU ignores the end wall effects, and continues to grow.

We believe that the physical content of the arguments of §2 has been substantiated.

5. CONCLUSIONS

The main points of the paper can now be summarized. First, we have shown that the fractal dimension is a useful concept for estimating the area of complex surfaces in turbulent flows, and that with this knowledge, specific arguments can be produced to estimate to within a constant (which itself can be, and has been, estimated separately) the fluxes of transportable quantities (such as mass, momentum and energy) across such surfaces. Second, it follows from Reynolds number similarity (ignoring intermittency effects) that the fractal dimension of interfaces in turbulent flows is $\frac{7}{3}$; an interesting interpretation is that the turbulent surfaces at the 'microscopic' level adjust themselves in such a way that the 'macroscopic' fluxes are independent of the fluid viscosity. The $\frac{7}{3}$ estimate is modified only slightly upward (to about 2.36) if we allow in a reasonable fashion for the fluctuations in the interface thickness and its propagation velocity. The corrected estimate is in excellent agreement with our previous as well as present experimental results. Third, we presented data as well as an analysis on the Reynolds number variation of the fractal dimension in developing flows. Fourth, we invoked the Schmidt number independence of mixing to show that the scale convolutions in the range $\eta > r > \eta_b$ are space filling. Finally, the prediction concerning the variation of mixing with the flow Reynolds number has been checked in some detail in a countercurrent shear flow.

We believe that the general procedure introduced in §2, which basically consists

in relating turbulent mixing and entrainment to molecular diffusion across a (non-static) fractal interface, is a self-consistent approach leading to an improved understanding and modelling of turbulent transport processes. We should re-emphasise our earlier statement in §2 that we do not either ignore or consider negligible the importance of the large-scale structure in initiating the transport. We have taken the view that one can examine a process as convincingly at the stage of its consummation as at the stage of initiation. We claim that it is much more tractable to understand and predict the process if we concentrate on the last stages, and have provided a self-consistent framework that is independent of the configurational details of the flow. It appears to us that many known features of mixing and entrainment can be explained within this framework.

Finally, we note the similarity of purpose between the present effort and that of Hentschel & Procaccia (1984) who, using an entirely different set of arguments, attempt to explain Lovejoy's (1982) result for the fractal dimension for cloud boundaries.

We are grateful to B. T. Chu, Peter Bradshaw, Gene Broadwell, Martin Maxey, and Ron Roy for commenting on the draft version of the manuscript, and to R. Prasad for his help on several matters related to data processing. We were helped in focusing our thoughts better by the comments of one of the referees. This work was supported by grants from AFOSR and DARPA.

APPENDIX A

We recall that one of our assumptions leading to equations (2.11) and (2.12) was that the dissipation rate averaged only over the interface region is equal to that averaged globally. To examine this, we study here the behaviour of the dissipation rate in the neighbourhood of the interface. For definiteness, let us divide the three dimensional domain of the flow in equal cubes of size r . Let us call ϵ_r the dissipation averaged in such a box. Clearly the global average of dissipation $\langle \epsilon \rangle$ will be given by considering very large cubes. On the other hand, the average of the dissipation along the interface $\langle \epsilon_\eta \rangle_i$ can roughly be obtained by using very small boxes of size comparable to the Kolmogorov scale η , and considering only the boxes which contain any part of the interface in performing the average. If we want to measure $\langle \epsilon_r \rangle_i$, the dissipation that occurs in a strip of thickness r along the interface, we can use boxes of size r and again only consider those which contain the interface.

Because we do not know *a priori* where in three dimensions the interface resides, we resort to the method of intersections used in I and described briefly in §4.2. In the context of scalar interfaces in turbulent flows, the method reduces to taking a slice of the flow (for example, by illuminating a dyed flow with a sheet of light of thickness comparable to the Kolmogorov scale), and examining the cut of the interface made by the light sheet. By working on the intersected plane, one determines the properties of the surface in three dimensions using the addition principle (see text).

We have so far not been able to obtain a two-dimensional cut of ϵ (because it

has nine non-zero components), but have made progress with respect to χ , the scalar dissipation field of the dye concentration c , for example. Noting that

$$\chi = (dc/dx)^2 + (dc/dy)^2 + (dc/dz)^2, \quad (\text{A } 1)$$

with x , y and z representing the cartesian coordinates, we can easily obtain the first two terms of χ , by centre differencing (for example) the concentration c with respect to both x and y in the plane of intersection. (The quantity c itself is available to us in the form of a digitized image on a CCD array of approximately 1300×110 pixels; note that the light intensity of the image is directly proportional to the concentration of the dye.) We shall assume that the average behaviour of the sum of the first two terms in (A 1) will adequately represent that of the entire χ . Prasad *et al.* (1988) have in fact tested this idea, and found it to be valid. To put the matter in perspective, we note that the first term alone is quite often used in the literature to represent the statistical behaviour of the sum of the three terms.

We have plotted in figure A 1 the variation of $\langle \chi_r \rangle_i$ (normalized by using the global average) with respect to r/η . It is clear that the variation is not large. The difference between the dissipation occurring in a strip of thickness η along the interface and the global average is not larger than 5%. The decrease of $\langle \chi_r \rangle_i$ with respect to r for $r/\eta < 30$ is understandable if we realize that interfaces are regions of marginally larger dissipation than the average nearby. But as one begins to include larger areas of the flow field (that is, as one begins to include the fully turbulent regions) the average goes up somewhat, and eventually converges to the global mean.

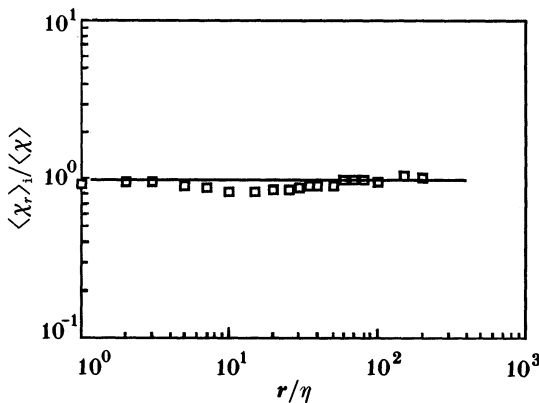


FIGURE A 1. Averages of the dissipation of concentration fluctuations χ , over regions of varying thickness r along the interface. The continuous line corresponds to the global average.

The upper part of figure A 2 shows the dissipation rate χ along a typical one-dimensional cut of the flow, and the corresponding points where the interface resides are shown in the lower part. It is seen that there is no clear correlation between the magnitude of χ and the interface. The main point then is that the use of the global mean $\langle \chi_r \rangle$ in place of $\langle \chi_r \rangle_i$, or $\langle \epsilon_r \rangle$ in place of $\langle \epsilon_r \rangle_i$, is a reasonably valid procedure.

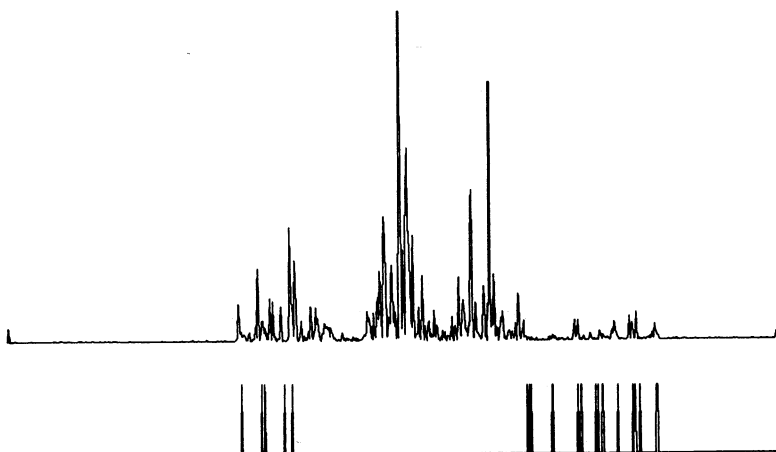


FIGURE A 2. Variation of the magnitude of χ along a typical one-dimensional cut through the flow-field. In the lower part, the points where the same cut intersects the interface are shown by vertical spikes.

As shown in §3, quarter powers of ϵ_r are also of special interest. We have plotted in figure A 3 the average of $\chi^{\frac{1}{4}}$ on boxes of varying size r . This was done along the interface, as well as in the whole turbulent region. Again, both situations are quite similar and (extrapolating to ϵ) the use of $\langle \epsilon^{\frac{1}{4}} \rangle$ instead of $\langle \epsilon^{\frac{1}{4}} \rangle_i$ appears to be a valid procedure.

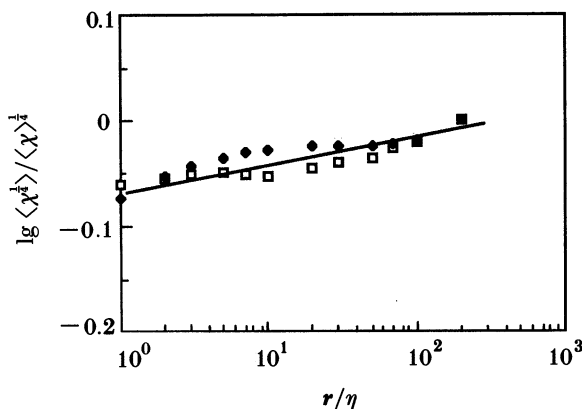


FIGURE A 3. Averages of $\chi^{\frac{1}{4}}$ on boxes of size r . Open symbols correspond to averages taken only using boxes along the interface, and closed symbols correspond to averages taken using boxes in the whole turbulent region.

APPENDIX B

Here, we estimate the constants β in equations (2.15a, b).

The mixing layer

We define, as usual, the entrainment velocity as

$$V_e = (d/dx) \int_{-\delta}^{\delta} u dy,$$

with 2δ as the thickness of the entire mixing layer, for example, the distance over which 99.5% of the velocity variation occurs. It follows that

$$\beta = (d/dx) \int_{-\delta}^{\delta} (u/\Delta U) dy.$$

From the experimental data of Wygnanski & Fiedler (1970), corresponding to $R = (U_1 - U_2)/(U_1 + U_2) = 1$, U_1 and U_2 being the two free stream velocities, we get $\beta = 0.15$. For non-unity R one can expect similar variation of the entrainment velocity with the velocity difference ΔU . Thus the parameter β would be independent of R .

The wake

Again defining the entrainment velocity as above, we get

$$V_e/U_0 = d/dx(2\delta - \delta^*),$$

where

$$\delta^* = \int_{-\delta}^{\delta} w/U_0 dy = w_0 \delta_{\frac{1}{2}}/U_0 \int_{-\delta}^{\delta} w/w_0 d(y/\delta_{\frac{1}{2}}) = (w_0/U_0) \delta_{\frac{1}{2}} I_1, \quad \text{say.}$$

Here, U_0 is the free stream velocity, w is the defect velocity (w_0 being its maximum) and $\delta_{\frac{1}{2}}$ is the half-wake thickness. From the evaluation of experimental data, Sreenivasan & Narasimha (1982) concluded that I_1 is a constant = 2.06, and so we can write

$$V_e/U_0 = (d/dx) (2\delta - (w_0/U_0) \delta_{\frac{1}{2}} I_1). \quad (\text{B } 1)$$

From many experiments, $2\delta = 5\delta_{\frac{1}{2}}$ approximately, so that

$$V_e/U_0 = (d/dx) \{ \delta_{\frac{1}{2}} [5 - (w_0/U_0) I_1] \}. \quad (\text{B } 2)$$

In the far-wake region, w_0/U_0 is rather small, of the order of a few percent. Neglecting the second term in (B 2), one gets after a little algebra, that

$$V_e/w_0 = 2.5 (\Delta/W),$$

where $\Delta = \delta_{\frac{1}{2}}/(x\theta)^{0.5}$, and $W = (w_0/U_0)(x/\theta)^{0.5}$. Here θ is the wake momentum thickness. Sreenivasan & Narasimha have shown that the quantities Δ and W are constants in the far-wake region, equal to 0.3 and 1.63 respectively. Although it is not entirely clear whether these numbers are universal in the far-wake region, that they attain constant values in the far-wake region, and that these constant values do not vary by more than 20% from one flow to another, seems quite clear.

Because we are not concerned here with too much precision, we may use the values quoted above, and conclude that

$$V_e/w_0 = 0.46,$$

yielding the constant β in (2.15a) to be about 0.46 for plane wakes. Similar calculations, although not given here, are quite straightforward for the plane and round jets, and the final results can be found in table 2. The boundary-layer case, being somewhat different, is presented below.

The turbulent boundary layer

Approximating the velocity distribution in a turbulent boundary layer by

$$U/U_0 = (y/\delta)^{1/n},$$

we may write the entrainment velocity V_e as

$$V_e/U_0 = (d/dx)[(2+n)\theta],$$

where

$$\theta \text{ is the momentum thickness} = \delta \int_0^1 u/U_0(1-u/U_0) d(y/\delta).$$

To a first approximation, n can be considered a constant, equal to about 7, so that

$$V_e/U_* = 9u_*/U_0.$$

The constant β in (2.15b) is thus of order 10, in excellent agreement with the correlation based on experiment of Bradshaw *et al.* (1967).

REFERENCES

- Batchelor, G. K. & Townsend, A. A. 1949 *Proc. R. Soc. Lond. A* **199**, 238.
 Bradshaw, P., Ferris, D. H. & Atwell, N. P. 1967 *J. Fluid Mech.* **28**, 593.
 Breidenthal, R. E. 1978 *A chemically reacting turbulent shear flow*. Ph.D. thesis, California Institute of Technology.
 Broadwell, J. E. & Breidenthal, R. E. 1982 *J. Fluid Mech.* **125**, 397.
 Corrsin, S. 1964 *Physics Fluids* **7**, 1156.
 Corrsin, S. & Kistler, A. L. 1955 *NACA Tech. Rept no.* 1244.
 Frisch, U. & Parisi, G. 1985 In *Turbulence and predictability in geophysical fluid dynamics and climate dynamics* (ed. M. Ghil, R. Benzi & G. Parisi), p. 84. New York: North-Holland.
 Henschel, H. G. E. & Procaccia, I. 1983 *Physica D* **8**, 435.
 Henschel, H. G. E. & Procaccia, I. 1984 *Phys. Rev. A* **29**, 1461.
 Kolmogorov, A. N. 1962 *J. Fluid Mech.* **13**, 82.
 Konrad, J. H. 1976 *An experimental investigation of mixing in two-dimensional turbulent shear flows with applications to diffusion-limited chemical reactions*, Ph.D. thesis, California Institute of Technology.
 Koochesfahani, P., Dimotakis, P. E. & Broadwell, J. E. 1984 *AIAA J* **22**, 1191.
 Koop, C. G. & Browand, F. K. 1979 *J. Fluid Mech.* **93**, 135.
 Lovejoy, S. 1982 *Science, Wash.* **216**, 185.
 Mandelbrot, B. B. 1974 *J. Fluid Mech.* **62**, 331.
 Mandelbrot, B. B. 1982 *The fractal geometry of nature*. San Francisco: Freeman.
 Meneveau, C. & Sreenivasan, K. R. 1987 *The Physics of Chaos and Systems Far From Equilibrium* (ed. Minh Doung-Van), *Nucl. Phys. B, Proc. Suppl.* **2**, p. 49. Amsterdam: North-Holland.
 Prasad, R. R. & Sreenivasan, K. R. 1988 *Experiments Fluids* (In the press.)

108 K. R. Sreenivasan, R. Ramshankar and C. Meneveau

- Prasad, R. R., Meneveau, C. & Sreenivasan, K. R. 1988 *Phys. Rev. Lett.* **61**, 74.
Ramshankar, R. 1988 *Dynamics of countercurrent mixing layers*. Ph.D. thesis, Yale University.
Roshko, A. 1976 *AIAA JI* **14**, 1349.
Sreenivasan, K. R. & Meneveau, C. 1986 *J. Fluid Mech.* **173**, 357.
Sreenivasan, K. R. & Narasimha, R. 1982 *J. Fluid Engng* **104**, 167.
Sreenivasan, K. R., Prabhu, A. & Narasimha, R. 1983 *J. Fluid Mech.* **137**, 251.
Tennekes, H. 1968 *Physics Fluids* **11**, 669.
Thorpe, S. A. 1968 *J. Fluid Mech.* **32**, 693.
Thorpe, S. A. 1971 *J. Fluid Mech.* **46**, 299.
Tong, P. & Goldburg, W. I. 1988 *Physics Lett. A* **127**, 147.
Wynanski, I. & Fiedler, H. 1969 *J. Fluid Mech.* **38**, 577.
Wynanski, I. & Fiedler, H. 1970 *J. Fluid Mech.* **41**, 327.

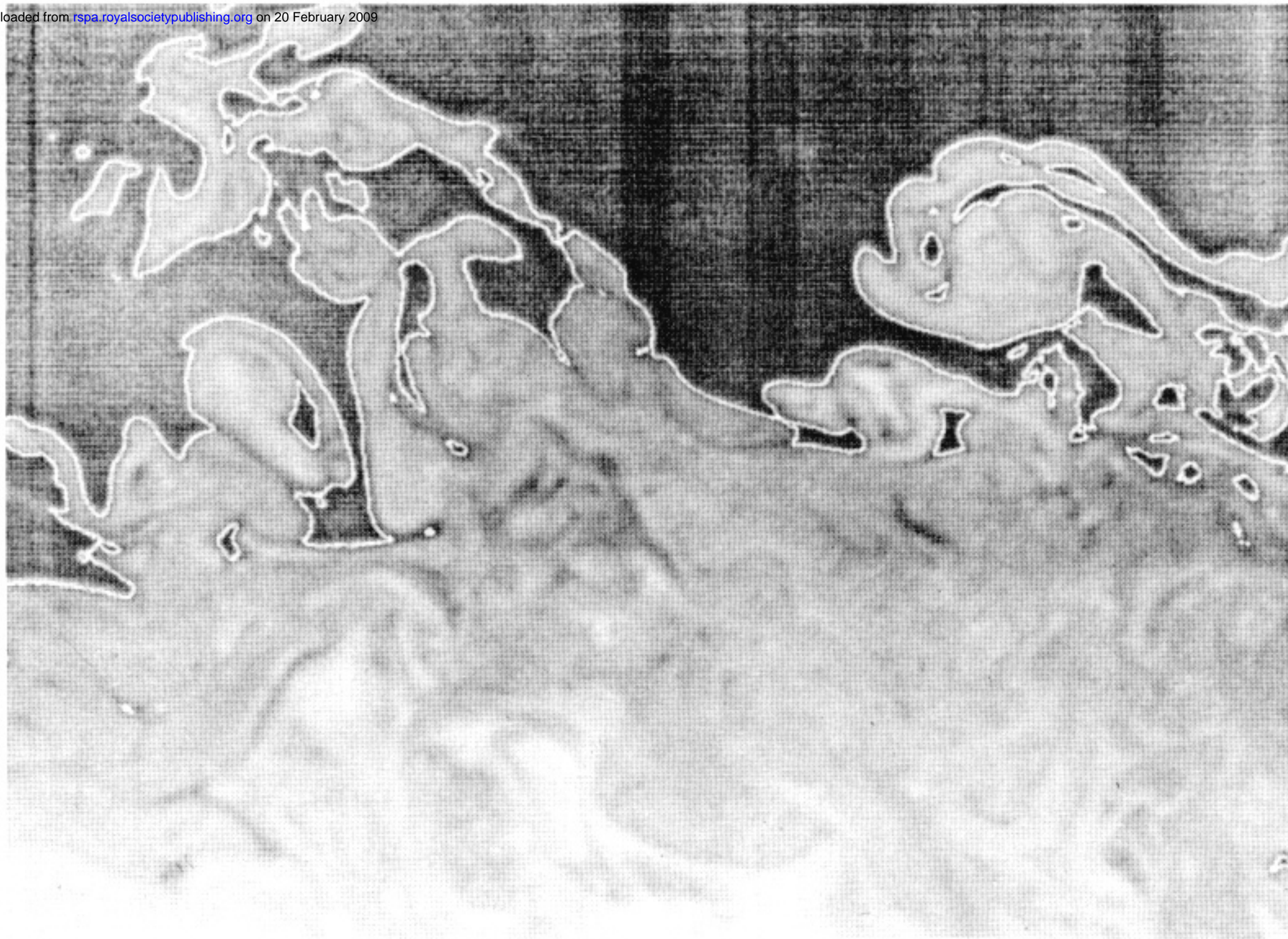
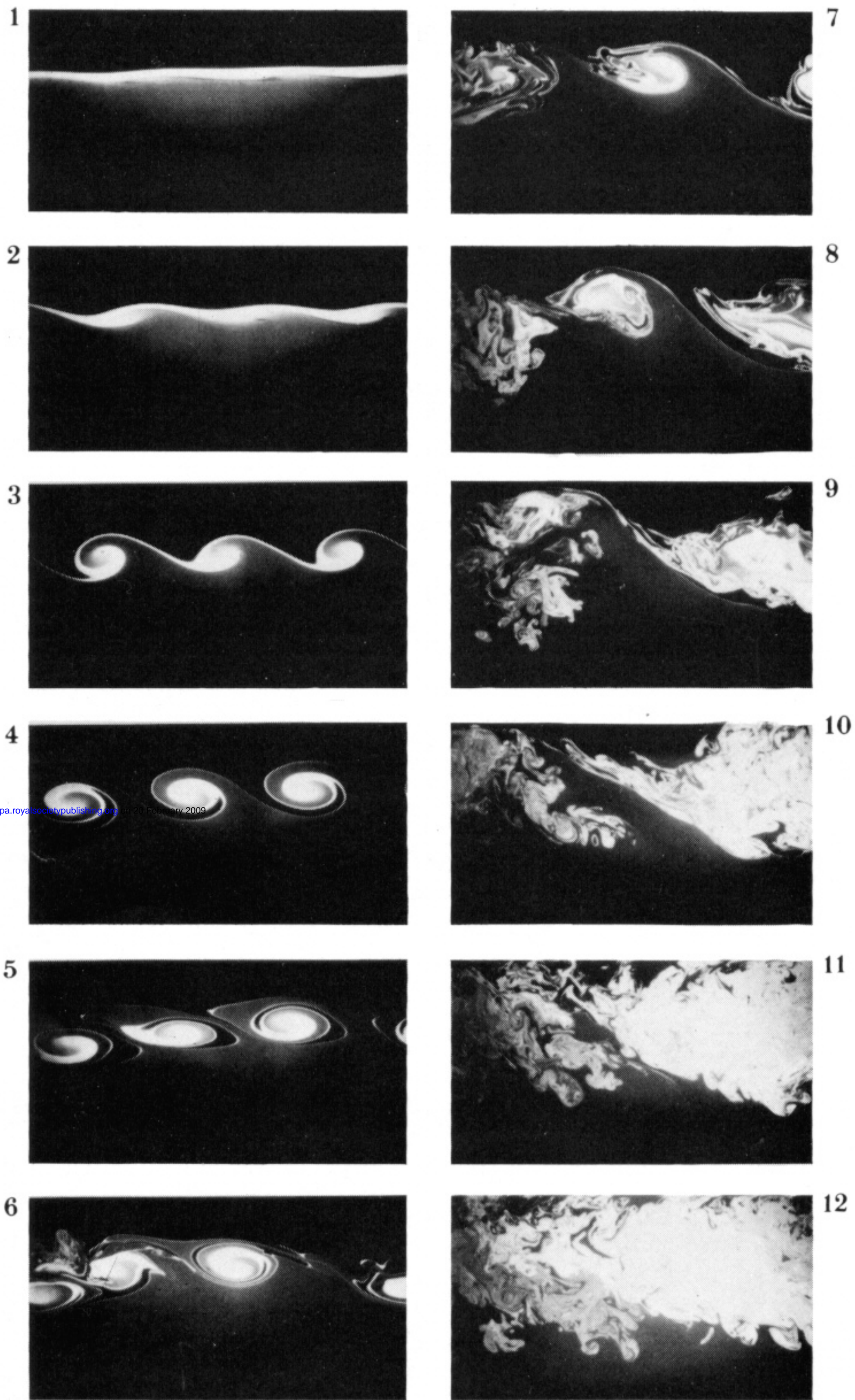


FIGURE 11. Section of a countercurrent flow at a moderate Reynolds number, obtained by using laser-induced fluorescence. Also shown as the white line is the interface drawn by setting a suitable threshold to demarcate the bright regions from the dark.



Downloaded from rspa.royalsocietypublishing.org/ on 20 February 2009

FIGURE 13. Visualization of a thin section of the countercurrent shear flow by laser induced fluorescence at different stages of its evolution. The numbers on these pictures correspond to those on the product thickness curve of figure 17 to follow. Unlike in figure 11, the dye was placed carefully in a thin sheet between the two fluids when filling the tube.